



**HAL**  
open science

## **Mechanosensitivity of cancer cells in contact with soft substrates using AFM**

Y. Abidine, A. Constantinescu, V. M. Laurent, V. Sundar Rajan, R. Michel,  
V. Laplaud, A. Duperray, Claude Verdier

► **To cite this version:**

Y. Abidine, A. Constantinescu, V. M. Laurent, V. Sundar Rajan, R. Michel, et al.. Mechanosensitivity of cancer cells in contact with soft substrates using AFM. *Biophysical Journal*, 2018, 114 (5), pp.1165-1175. 10.1016/j.bpj.2018.01.005 . hal-01615377v2

**HAL Id: hal-01615377**

**<https://hal.science/hal-01615377v2>**

Submitted on 19 Dec 2017

**HAL** is a multi-disciplinary open access archive for the deposit and dissemination of scientific research documents, whether they are published or not. The documents may come from teaching and research institutions in France or abroad, or from public or private research centers.

L'archive ouverte pluridisciplinaire **HAL**, est destinée au dépôt et à la diffusion de documents scientifiques de niveau recherche, publiés ou non, émanant des établissements d'enseignement et de recherche français ou étrangers, des laboratoires publics ou privés.

# Mechanosensitivity of cancer cells in contact with soft substrates using AFM

Y. Abidine,<sup>1</sup> A. Constantinescu,<sup>3</sup> V.M. Laurent,<sup>1</sup> V. Sundar Rajan,<sup>2</sup>  
R. Michel,<sup>1</sup> V. Laplaud,<sup>1</sup> A. Duperray,<sup>2</sup> and C. Verdier<sup>1,\*</sup>

<sup>1</sup>Univ. Grenoble Alpes, CNRS, LIPhy, 38000 Grenoble, France

<sup>2</sup>Institute for Advanced Biosciences, INSERM U 1209, CNRS UMR 5309, Univ. Grenoble Alpes, 38000 Grenoble, France

<sup>3</sup>École Polytechnique, CNRS, Laboratoire de Mécanique des Solides, 91128 Palaiseau, France

## Abstract

Cancer cells are usually found to be softer than normal cells. But their stiffness changes when they are in contact with different environments, due to mechanosensitivity. For example, they adhere to a given substrate by tuning their cytoskeleton, thus affecting their rheological properties. This mechanism could become efficient when cancer cells invade the surrounding tissues, and they have to remodel their cytoskeleton in order to achieve particular deformations. Here we use an atomic force microscope (AFM) in force modulation mode to study how local rheological properties of cancer cells are affected by a change of the environment. Cancer cells are plated on functionalized polyacrylamide substrates of different stiffnesses, as well as on an endothelium substrate. A new correction of Hertz model is developed because measurements require to account for the precise properties of the layered, thin viscoelastic substrates. The main results show the influence of local cell rheology (nucleus, perinuclear, edge locations), and the role of invasiveness. A general mechanosensitive trend is found where the cell elastic modulus and transition frequency increase with substrate elasticity, but this tendency breaks down with a real endothelium substrate. These effects are investigated further during cell transmigration, when the actin cytoskeleton undergoes a rapid reorganization process necessary to push through the endothelial gap, in agreement with the local viscoelastic changes measured by AFM. Taken together, these results introduce a paradigm for a new possible extravasation mechanism.

*Submitted May 22, 2017, revised December 19, 2017.*

\*Correspondence: [claude.verdier@univ-grenoble-alpes.fr](mailto:claude.verdier@univ-grenoble-alpes.fr)

Keywords: AFM, cancer cells, viscoelasticity, transendothelial migration

Running title: Mechanosensitivity of cancer cells

## INTRODUCTION

The role of cell mechanics has been investigated a lot in recent years, and is essential in many biological phenomena based on the cell ability to modify its shape and cytoskeleton, and therefore its rheology. These changes are important during embryogenesis, cell division, cell migration, metastasis or the epithelial–mesenchymal transition, to mention just a few processes. Therefore the investigation of cell mechanics has become a major issue, and has led to the development of specific tools to

study cell (visco)elasticity, such as optical tweezers, optical stretchers, microplates, micropipettes, magnetic twisting cytometry, atomic force microscopy (AFM), microbead tracking with laser or light, to investigate cell internal microrheological properties (1).

Due to the variety of possible ways to investigate cell mechanics, different cell types have been tested, in particular metastatic cancer cells were studied extensively (2) and seem to become softer as they pass from blood through the endothelium (3) to invade new tissues (4). More precisely,  $E$ , the elastic Young modulus of cells, seems to decrease when cells become invasive as compared to normal ones (5–7). This concept is not always admitted, as cells may require more stiffness to break through a biological tissue, as shown recently by combining AFM and confocal microscopy (8). One way to answer this question is to study the cytoskeleton, a complex dynamic system, involving acto–myosin contractile elements, intermediate filaments and microtubules (9–11). The cytoskeleton is both locally and mechanically heterogeneous (12). In particular, the region on top of the nucleus of adherent cells or the perinuclear part, can exhibit significantly different mechanical properties, as compared to protrusions or filopodia (13, 14). Finally the nucleus plays a role in cell elasticity (15), as its deformability is a prerequisite to squeeze through complex confined networks (16). Another important parameter is viscosity, which can be quite relevant (17) because of the viscous components of the cell cytoplasm and could be a potential marker of cancer cells (18).

Recently, studies focusing on the environment revealed important strategies used by cells to remodel their cytoskeleton, a process known as mechanosensing. Indeed cells can adapt their response when the substrate has changing stiffness (19), or migrate towards a more rigid substrate (20), where they spread and reinforce their focal adhesions (21). Cell spreading also increases on thinner gels, since they feel the substrate below (22). Cells also adapt their stiffness according to the substrate elasticity (23). When in contact with substrates of rapidly increasing stiffness, they develop larger forces via remodeling of the acto–myosin cortex (24). Regarding the particular case of cancer cells, it has been shown that human breast cancer invasion correlates with a stiffening of the surrounding Extra Cellular Matrix (ECM) depending on cell–type, matrix, integrins, or collective effects (25, 26). Cancer cell invasiveness seems to be linked with the way cells sense or indent elastic gels, so it could be a good tool to distinguish them (27). Further works showed that the heterogeneity of complex matrigels mimicking the microenvironment can promote cancer cell invasion (28). In tumors, cells remodel the ECM around them to force progression (29, 30). This change in force generation has been studied using traction force microscopy in 2D and 3D (31–33) but is not yet related so clearly to the cytoskeleton of cancer cells.

To investigate the cell microrheological properties, an AFM in force modulation mode (14, 17, 34, 35) is particularly well adapted. Despite the commonly available AFM softwares or home–made systems, few results have focused on the role of the environment on cell viscoelastic properties. Thus, in this work, we consider the effect of an elastic substrate on the mechanical properties of adhering cancer cells, and evaluate their mechanosensitivity. This is carried out for three different elastic gels ( $E$  ranging from 5 kPa to 28 kPa), and an endothelium substrate. Microrheological properties (36) are obtained in a large frequency range [1–500 Hz]. Since substrates are thin and viscoelastic, a three–layer model, inspired from previous

work (37), is used to account for substrate effects. Finally, using a viscoelastic model (14), two main parameters are identified, corresponding to the signature of cancer cells, namely  $G_N^0$ , the elastic plateau modulus and  $f_T$ , the transition frequency from elastic to glassy state (38). The evolution of these parameters shows surprising changes in the case of invasive cancer cells on the endothelium substrate. This is confirmed by separate transmigration experiments, showing that rapid cytoskeleton reorganization is necessary to cross the endothelial barrier.

## MATERIALS AND METHODS

### Cell culture

Cancer cells – Three epithelial bladder cancer cell lines, representing increasing malignancy states of metastasis progression, were used, RT112, T24 and J82 (ATCC, Rockville, MD). RT112 cancer cells are moderately differentiated while T24 and J82 cancer cells are poorly differentiated and have a higher malignancy potential (especially J82 cells). The choice of these bladder cell lines comes from earlier studies by the authors (39–41). Cell lines are classified according to the corresponding tumor they were taken from, using the Tumor–Node–Metastasis system (TNM system – UICC 2009). T stands for the stage and describes how far the primary tumor has grown into the bladder ( $T_0$ – $T_4$ ). The majority of bladder cancers is linked to non–invasive papillary tumors of lower grade ( $T_a$ ). N is the spread to lymph nodes near the bladder ( $N_0$ – $N_3$ ) and M is the spread of the tumor to other parts of the body ( $M_0$ ,  $M_1$ ). This information is combined to give the overall stage ( $G_0$ – $G_4$ ). According to these standards, RT112 (German tumorbank, luminal molecular subtype) is a  $T_a$ – $G_2$  cell type. T24 (ATCC-HTB-4, luminal/basal molecular subtype) is a more invasive cell line ( $T_2$ – $G_3$ ). J82 (ATCC-HTB-1, luminal/basal molecular subtype) is a very invasive cell line ( $T_3$ – $G_3$ ). Taken together, this gives a wide variety of invasiveness.

These cells were cultured in RPMI 1640 (Gibco, Saint-Aubin, France) supplemented with 10% fetal calf serum and 1% penicillin streptomycin. One day before measurements, cells were seeded at a density of  $3.0 \cdot 10^4$  cells per well on gels coated with 20  $\mu\text{g}/\text{mL}$  fibronectin (Promocell, Heidelberg, Germany) overnight at  $37^\circ\text{C}$  in humidified 5%  $\text{CO}_2$  atmosphere. Such cells are considered to have a low migrating velocity since the fibronectin concentration is quite high (42). AFM measurements were carried out on isolated cells at  $37^\circ\text{C}$ . Cancer cells were transfected with the LifeAct plasmid expressing actin-GFP (Green Fluorescent Protein-pEGFP).

Endothelial cells – Human Umbilical Vascular Endothelial Cells (HUVECs) purchased from Promocell (Heidelberg, Germany) were plated in complete culture medium (Promocell) on glass coverslips coated with fibronectin (10  $\mu\text{g}/\text{mL}$ ) and left 3 days at  $37^\circ\text{C}$  in humidified 5%  $\text{CO}_2$  atmosphere to spread and achieve confluence.

### Cell transendothelial migration

To verify the results postulated with the AFM, and understand how a change in substrate can affect the cytoskeleton of cancer cells during transmigration, an experiment was carried out, using cancer cells in contact with a HUVEC monolayer grown

on a gel of elasticity 8kPa. A stamping procedure was used with a patterned PDMS block functionalized with fibronectin (25  $\mu\text{g}/\text{mL}$ ). Stamps were put in contact with gels for one hour, then were gently removed (43). Endothelial cells (HUVECs) were seeded in complete culture medium (Promocell) overnight to form a monolayer on the circular 80  $\mu\text{m}$ -patterns. Finally invasive cancer cells (J82) were put in solution and let to sediment. As many patterns were used in parallel, cases with one single cancer cell adhering and transmigrating through the HUVEC monolayer could be followed. J82 cells were transfected for actin-GFP so that the actin cytoskeleton could be visualized on the confocal microscope (Zeiss, LSM, Germany). HUVECs were stained with CellTrace Far Red DDAO-SE (Life technologies) to observe their shape. The microscope was equipped with multiwave acquisition (green and red) and a chamber to maintain 37°C and supply 5% CO<sub>2</sub> for the cells. After cancer cells had sedimented, they came in contact with the endothelial cells, found their way through the cell-cell junctions, then passed through and spread below. Fluorescence was used to visualize cancer cells and endothelial cells at the same time.

### Gel preparation

PolyAcrylAmide (PAA) gels were prepared following a previous protocol (43). Three gels containing OH bonds, enabling easy functionalization using fibronectin (20  $\mu\text{g}/\text{mL}$ ), were prepared by mixing acrylamide (30% w/w), N-Hydroxyethylacrylamide (N-HEA, 5.85% w/w) and N,N-methylene-bisacrylamide (2% w/w) in different amounts (Sigma-Aldrich, Saint Quentin-Fallavier, France). Three concentrations of bisacrylamide were used (0.1–0.3–0.6 %) whereas the acrylamide (3.2%), and N-HEA (1.25%) contents were fixed in the final 50 mM HEPES solution. Polymerization was initiated by incorporating N,N,N,N-tetramethylethylene-diamine (TEMED, Sigma) and ammonium persulfate 10% solution (APS, Sigma-Aldrich). 70  $\mu\text{m}$ -thick gels were prepared on a pre-treated glass Petri dish for better adhesion. After polymerization, samples were indented using AFM in contact mode, or characterized using a rheometer to obtain the plateau modulus  $G_N^0$  (30). Since viscous effects were negligible, one could assume that  $E \sim 3G_N^0$ . Both measurements agreed, with gel moduli  $E \sim 5 \pm 1$  kPa,  $8 \pm 1.5$  kPa and  $28 \pm 3$  kPa. Gels were kept under humid conditions before cell seeding.

### AFM measurements

Experiments were carried out using a Nanowizard II AFM (JPK Instruments, Berlin, Germany) mounted on a Zeiss microscope (Observer D1, Carl Zeiss, Jena, Germany). All measurements were conducted in Force Modulation Mode at 37°C using the Petri Dish Heater (JPK Instruments, Berlin, Germany). We used triangular silicon nitride cantilevers with four-sided pyramidal tips (MLCT, lever C, Bruker, Camarillo, CA, USA) with a nominal spring constant  $k \sim 0.01$  N m<sup>-1</sup> calibrated using the thermal noise method (44). Sharp tips are better suited to reach a higher spatial resolution. The applied force was lower than 2 nN in order to deform the substrate within the linear elastic regime where the Hertz indentation model can be used. When the cantilever tip gets into contact with the sample, the force acting on the cantilever increases to a previously chosen

setpoint  $F$ , corresponding to an initial indentation  $\delta$ . The relationship is given by Sneddon's modification of the Hertzian contact mechanics model (45):

$$F = \frac{3 E \tan \theta}{4(1 - \nu^2)} \delta^2 = \frac{3}{4} \bar{E} \tan \theta \delta^2 \quad (1)$$

where  $E$  is the cell's Young modulus,  $\nu$  its Poisson ratio ( $\nu \sim 0.5$ ),  $\bar{E} = E/(1 - \nu^2)$  is the apparent modulus and  $\theta = 20^\circ$  is the half pyramid angle.

AFM measurements were carried out at different geometrical locations, namely N, P and E (14). N designates a location on top of the nucleus, this does not mean that the nucleus is measured, since it is known that actin cytoskeleton may be present in the thin layer between the nucleus and the cell membrane. P is usually located 10  $\mu\text{m}$  away from the nucleus geometrical center. Finally, E represents the edge of the cell, typically 5  $\mu\text{m}$  from the edge. These locations can be seen on the sketch in the insert of Fig. 1 B and in Fig. 2 C.

### Correction for indentation of a cell on a soft substrate: three-layer model

The precise analysis of the indentation experiment of a cell is highly dependent on its environment consisting of soft (gel or HUVEC monolayer) and hard substrates (glass dish). The Hertz formula (Eq. 1) is only valid as long as the indentation depth is small compared to sample thickness. The influence of the substrate grows with increasing indentation depth  $\delta$  and starts to be non-negligible at about one tenth of the substrate thickness  $h$  ( $\chi = \delta/h \sim 0.1$ ). This induces an overall strain of 10%, which is the accepted limit between small and large strains. More details on specific corrections have been proposed for spherical or pyramidal indenters (13, 36, 46). In the case of indentation on a *hard substrate*, the cell elastic modulus appears much higher than expected whereas, on a *soft gel*, the cell modulus seems to be smaller.

The analysis presented here is a generalization of the Hertz formula for indentation of a composite substrate using power law functionals. The numerical model employed is based on the Papkovitch–Neuber Potential representation of the displacement field, and has been verified on various hard and soft combinations of substrates with different axially symmetric indenter shapes (37, 47, 48). In the present experimental configuration, a cell (layer 1) is spread on a soft gel or HUVEC monolayer (layer 2) in contact with glass (layer 3). Let us call  $E_i, \nu_i, h_i$  the Young modulus, the Poisson ratio and the thickness respectively, where the indices  $i = 1, 2, 3$  denote the layers. Let us further remark that the glass substrate thickness is infinite ( $h_3 \rightarrow \infty$ ). This three-layer system is treated using power law functionals as detailed in the Appendix A of the Supporting Material, and has an apparent effective modulus:

$$\bar{E}_{(\delta)} = \bar{E}_3 + \frac{\bar{E}_2 + \frac{\bar{E}_1 - \bar{E}_2}{1 + (\frac{\delta}{\beta_0 h_1})^{\eta_0}} - \bar{E}_3}{1 + (\frac{\delta}{\beta_1 h_{12}})^{\eta_1}} \quad (2)$$

where  $h_{12} = h_1 + h_2$ , and  $\beta_0, \eta_0, \beta_1$  and  $\eta_1$  denote a series of shape parameters.

The model parameters  $\beta_0$ ,  $\eta_0$ ,  $\beta_1$  and  $\eta_1$  were obtained (see Fig. S2 in the Supporting Material) for relevant values of the cell modulus  $E_1$ , ranging from 1 kPa to 20 kPa, with gel modulus  $E_2$  taking values between 5 and 28 kPa, as in the experiments, and the stiffness of the glass substrate  $E_3$  was considered very large  $\sim 70$  MPa.  $h_1$ , the cell height, was measured experimentally on the nucleus, perinuclear region and cell edge.  $h_2$  equals 70  $\mu\text{m}$  for gels, and  $h_2 \sim 8 \mu\text{m}$  in the case of endothelial cells.

### Dynamic AFM measurements: $G'$ and $G''$

In order to carry out microrheology measurements, an initial indentation  $\delta_0$  was made, corresponding to the applied force  $F_0 = \frac{3}{4} \bar{E}_{(\delta_0)} \tan \theta \delta_0^2$  in Eq. 1. A small perturbation  $\delta(\omega)$  at angular frequency  $\omega$  ( $\omega = 2\pi f$  and the frequency  $f$  varies from 1 Hz to 500 Hz) was superposed to the initial indentation  $\delta_0$ . During this procedure the tip remained in contact with the cell. We imposed the indentation  $\delta(\omega)$  and measured the force response  $F(\omega)$  (17, 36). The perturbation being small, Eq. 1 was linearized around the equilibrium  $F_0 + F = \frac{3}{4} \bar{E}_{(\delta_0+\delta)} \tan \theta (\delta_0 + \delta)^2$ . At first order:

$$\frac{F}{\delta} \frac{2}{3 \tan \theta \delta_0} = \bar{E}_1 k_1(\chi_0, \chi_1) + \bar{E}_2 k_2(\chi_0, \chi_1) + \bar{E}_3 k_3(\chi_1) \quad (3)$$

where  $k_1$ ,  $k_2$ , and  $k_3$  are functions of the reduced indentations  $\chi_0 = \frac{\delta_0}{\beta_0 h_1}$ ,  $\chi_1 = \frac{\delta_0}{\beta_1 h_{12}}$  and parameters  $\eta_0$ ,  $\eta_1$  from Eq. 2 are investigated in the Appendix B of the Supporting Material:

$$\begin{cases} k_1(\chi_0, \chi_1) = \frac{2(1 + \chi_0^{\eta_0})(1 + \chi_1^{\eta_1}) - \eta_0 \chi_0^{\eta_0} (1 + \chi_1^{\eta_1}) + \eta_1 \chi_1^{\eta_1} (1 + \chi_0^{\eta_0})}{2(1 + \chi_0^{\eta_0})^2 (1 + \chi_1^{\eta_1})^2} \\ k_2(\chi_0, \chi_1) = \frac{2\chi_0^{\eta_0} (1 + \chi_0^{\eta_0})(1 + \chi_1^{\eta_1}) + \eta_0 \chi_0^{\eta_0} (1 + \chi_1^{\eta_1}) - \eta_1 \chi_1^{\eta_1} \chi_0^{\eta_0} (1 + \chi_0^{\eta_0})}{2(1 + \chi_0^{\eta_0})^2 (1 + \chi_1^{\eta_1})^2} \\ k_3(\chi_1) = \frac{\chi_1^{\eta_1} (2 + \eta_1 + 2\chi_1^{\eta_1})}{2(1 + \chi_1^{\eta_1})^2} \end{cases} \quad (4)$$

By the correspondence principle of linear viscoelasticity, one uses a complex indentation  $\delta^*$  and force  $F^*$ . The hydrodynamic viscous drag  $i\omega b(0)$  is subtracted from  $\frac{F^*(\omega)}{\delta^*(\omega)}$  as explained previously (14, 17).  $b(0)$  is estimated from the extrapolation of  $b(h)$  as a function of the tip-sample separation  $h$  to  $h = 0$ . For the sake of simplicity, it is not written in Eq. 5 which now reads, in complex form:

$$G^*(\omega) = G_1^*(\omega) = \frac{F^*(\omega)}{\delta^*(\omega)} \frac{1 - \nu_1}{3 \tan \theta \delta_0} \frac{1}{k_1} - E_2^* \frac{k_2}{k_1} \frac{1 - \nu_1}{2(1 - \nu_2^2)} - E_3^* \frac{k_3}{k_1} \frac{1 - \nu_1}{2(1 - \nu_3^2)} \quad (5)$$

where  $G^*(\omega) = G' + iG''$  is the required cell complex viscoelastic modulus. Note that  $E_2^*$  and  $E_3^*$  can be complex as well. This is the case with endothelial cells ( $E_2^*$ ). For the third layer (glass),  $E_3^* = E_3$  is real. The initial indentation  $\delta_0$  and heights  $h_1$  and  $h_{12}$  are known experimentally. We impose  $\delta_0 = 500$  nm,  $h_1 \sim 10 \mu\text{m}$  on the nucleus (N),  $\delta_0 = 400$  nm,  $h_1 \sim 1 \mu\text{m}$  on the perinuclear region (P) and  $\delta_0 = 100$  nm,  $h_1 \sim 200$  nm on the edge (E). Functions  $k_1(\chi_0, \chi_1)$ ,  $k_2(\chi_0, \chi_1)$  and  $k_3(\chi_1)$  are calculated using parameters  $\beta_0$ ,  $\eta_0$ ,  $\beta_1$  and  $\eta_1$  as explained in Appendix A of the Supporting Material. The procedure requires

an initial value of  $G_1^*(\omega)$  to start iterating (since  $k_1, k_2, k_3$  in Eq. 5 depend on  $G_1^*$ ) to find the new  $G^* = G_1^*$ . Convergence is verified when the relative error is smaller than 1%, usually after twenty iterations.

### Modeling $G'$ and $G''$

After obtaining experimental rheology data using correction formulae, it was found that in most cases  $G'$  is flat at low frequencies, then increases to reach a power law with slope  $a$ , in terms of  $\omega$ . On the other hand,  $G''$  decreases with slope  $-n_f$  at low frequencies, then increases as a power law with the same exponent  $a$ . A simple model (14) was proposed:

$$G'(\omega) = G_N^0 + g_1 \omega^a \quad (6)$$

$$G''(\omega) = k_0 \omega^{-n_f} + b g_1 \omega^a \quad (7)$$

where  $G_N^0$  is the so-called plateau modulus (Pa),  $a$  is the slope of  $G'$  and  $G''$  at high frequencies,  $b$  is the ratio  $\frac{G''}{G'}$  at high frequencies, and  $k_0$  and  $g_1$  are constants. Note that there exists a transition frequency  $f_T$  corresponding to crossing of  $G'$  and  $G''$  at the higher frequencies, given by  $f_T = \frac{1}{2\pi} \left( \frac{G_N^0}{(b-1)g_1} \right)^{1/a}$ . This model is slightly different from previous ones (17, 38) but assumes that universal power law behavior is not always met (49). In particular, at low frequencies, an elastic plateau modulus  $G_N^0$  is found. Parameters  $G_N^0$  and  $f_T$  will be used in what follows to quantify differences in cancer cell microrheological properties.

### Statistical analysis

Data was analyzed by a two-sample unpaired Student's t-test.  $n$  is the number of cells per condition. Values in Fig. 1–3–4–5 correspond to  $p < 0.001$  (\*\*\*),  $p < 0.01$  (\*\*),  $p < 0.05$  (\*) and  $p > 0.05$  (n.s.). Values were considered statistically significant when  $p < 0.05$ . Error bars in all figures represent the standard error of the mean (SEM).

## RESULTS

### Local microrheology depends on cell location and substrate stiffness

We first present results of the measurements made using T24 cancer cells on a soft gel ( $E_2 = 5$  kPa) and different locations are tested in Fig. 1 A–D. The contribution of the substrate has been taken into account. Both sets of data can be seen, with and without corrections. It is clear that the shear moduli  $G'$  and  $G''$  are affected by the presence of the substrate. Note also that the measurements depend on tip position. To clarify this, Fig. 1 D shows the modulus  $|G^*| = (G'^2 + G''^2)^{1/2}$  at 1.4 Hz, increasing as the point of measurement moves from the center (nucleus N) to the perinuclear region (P) and towards the lamellipodium (or edge E).



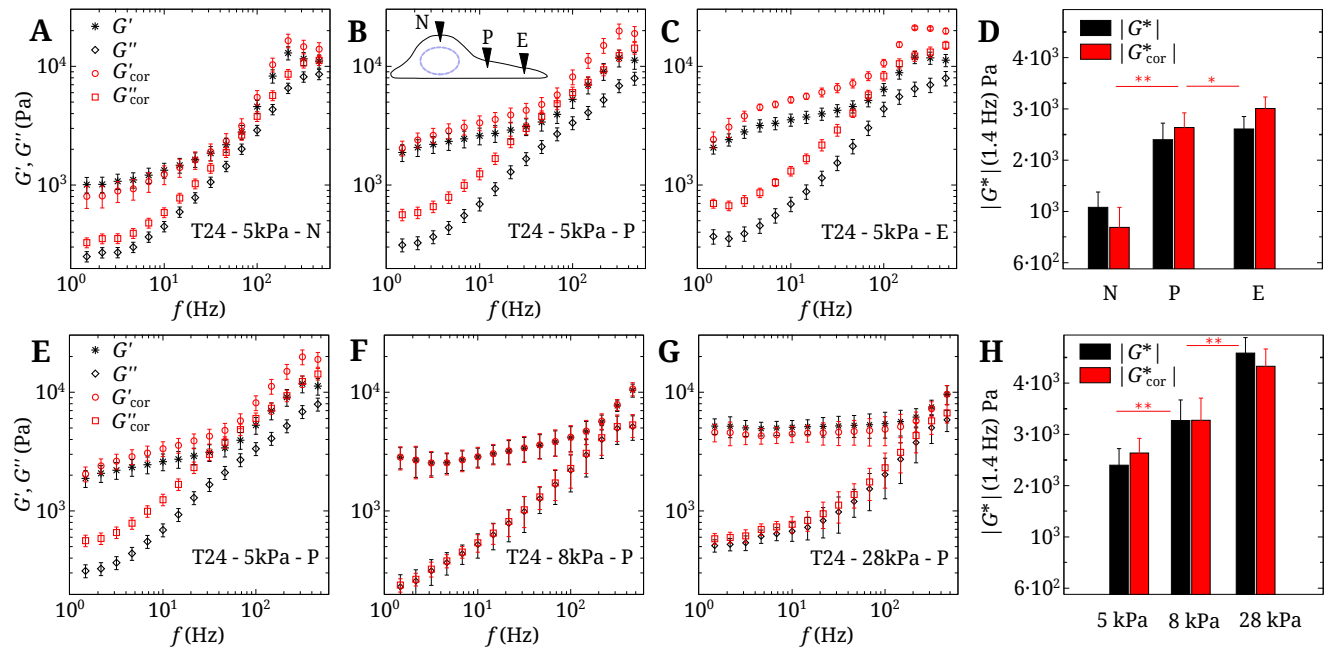


Figure 1: Raw and corrected viscoelastic moduli of T24 cells. (A–C) Data on a 5 kPa-gel at three locations N = Nucleus, P = Perinuclear region, E = Edge. (D) Modulus  $|G^*|(1.4 \text{ Hz})$  at the three locations N, P, E. (E–G) Data measured in the perinuclear region (P) on three gels  $E_2 = 5, 8, 28 \text{ kPa}$ .  $n = 5$ , error bars represent SEM. (H) Modulus  $|G^*|(1.4 \text{ Hz})$  for the three gels  $E_2 = 5, 8, 28 \text{ kPa}$ . Statistical relevance is shown for corrected values of  $|G^*|$ .

We next turn to the evolution of the dynamic moduli when substrate stiffness  $E_2$  is increasing. Three gels were used:  $E_2 = 5, 8, 28 \text{ kPa}$ . This is presented in Fig. 1 E–H. At low frequencies,  $|G^*|(1.4 \text{ Hz})$  increases when  $E_2$  increases, as seen in Fig. 1 H. This can be due to the cell actin microstructure or the spreading of cells on the substrate (14). In Fig. 2 A–C, T24 cells plated on PAA gels (5, 8, 28 kPa) are shown using confocal microscopy: they spread more, become thinner and develop more actin fibers on rigid gels. Note that the variation of  $|G^*|$  with  $E_2$  (Fig. 1 H), due to the thinning of cells and enhanced substrate effects, is less important after corrections are made. It can be concluded that the increase in cell elasticity comes rather from the cytoskeleton through creation of aligned actin fibers.

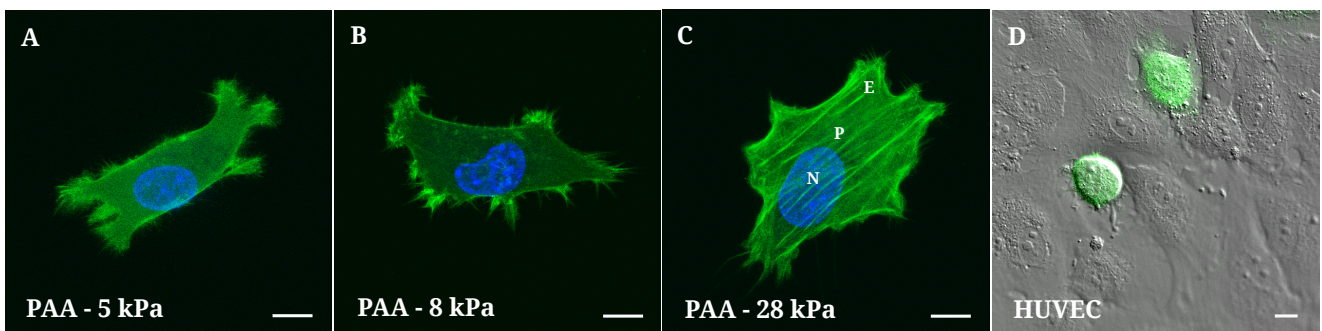


Figure 2: (A–C) Fluorescence of a GFP-actin T24 cells on three PAA substrates ( $E_2 = 5, 8, 28 \text{ kPa}$ ) with respective spreading areas  $863 \mu\text{m}^2$ ,  $1025 \mu\text{m}^2$  and  $1541 \mu\text{m}^2$  (D) DIC image of a HUVEC monolayer with green fluorescent T24 cells superimposed. Due to the round shape of the cells, it is not possible to define a lamellipodium or edge (E). Scale bar =  $10 \mu\text{m}$ .

### Cell microrheological properties are linked to cell invasiveness

The influence of invasiveness was studied next. Three cancer cells of increasing invasiveness (RT112 < T24 < J82) were plated on the 8 kPa PAA gel. Their viscoelastic properties are shown in Fig. 3 A–C, and display a common trend, with lower moduli  $G'$  and  $G''$  as the invasiveness increases. Substrate corrections are shown together with raw data. One can conclude that the microrheological properties of cancer cells depend on their invasiveness, i.e. moduli are lower for the more invasive cells. This is clearly shown for  $|G^*|(1.4 \text{ Hz})$  in Fig. 3 D. Such results were previously reported for the global elastic moduli  $E$  of cancer cells (5), their local elasticity (6, 7, 50) or viscoelasticity (14, 35). Note here that applying substrate corrections has a significant effect on the results.

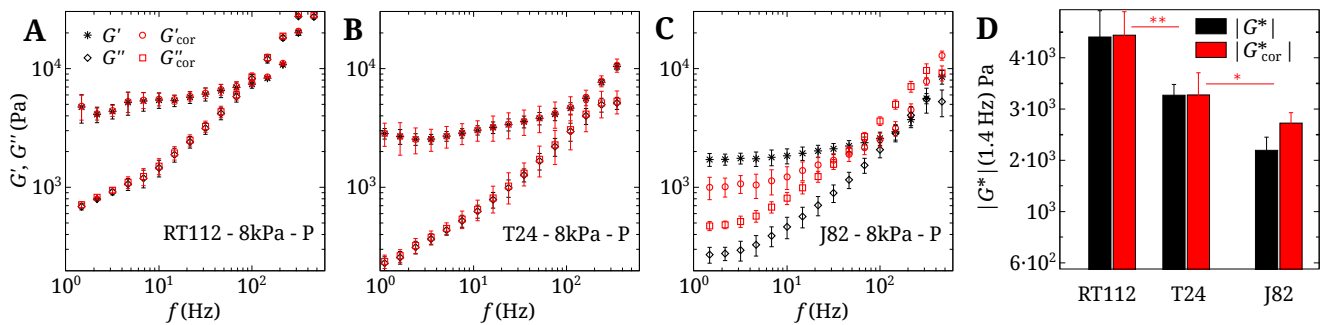


Figure 3: (A–C) Raw and corrected viscoelastic moduli of three cancer cells (RT112 – T24 – J82) on the 8 kPa gel.  $n=5$ , error bars represent SEM. (D) Corresponding values of  $|G^*|(1.4 \text{ Hz})$  for the three cell types. Statistical relevance is shown for corrected values of  $|G^*|$ .

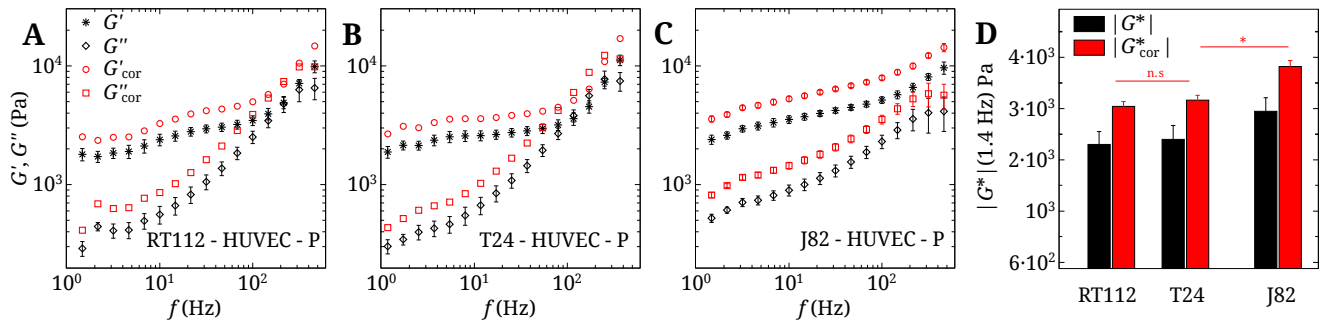


Figure 4: (A–C) Raw and corrected viscoelastic moduli of three cancer cells (RT112 – T24 – J82), measured in the perinuclear region (P), on a HUVEC monolayer.  $n = 5$ , error bars represent SEM. (D) Corresponding values of  $|G^*|(1.4 \text{ Hz})$  for the three cell types. Statistical relevance is shown for corrected values of  $|G^*|$ .

### Invasive cells exhibit an inverse behavior on the HUVEC substrate

We next characterize the behavior of the same cancer cells in contact with the endothelial monolayer. This layer has similar mechanical properties (51) as the 8kPa–PAA gel studied above. Therefore, one could wonder what effects can be found regarding cell spreading or cell viscoelasticity, and whether this could affect transendothelial migration. We find that, on the

HUVEC monolayer, cells do not spread much and remain round (Fig. 2 D) so it is hard to distinguish a lamellipodium (or edge E). Only measurements on the nucleus (N) and perinuclear region (P) were performed. Fig. 4 A–D shows these measurements on the perinuclear region (P). Note that corrections in Fig. 4 A–C use the real viscoelastic properties of endothelial cells, measured separately (51). In this case the viscoelastic properties of cancer cells show a different trend. Fig. 4 D summarizes the evolution of  $|G^*|(1.4 \text{ Hz})$  showing that more invasive cells are slightly stiffer in the perinuclear region. Finally, the crossover frequency  $f_T$  varies significantly. For J82 cells,  $f_T$  cannot be reported because this crossover is out of the range of frequencies used. In the next part we will compare quantitative numbers, such as  $G_N^0$  and  $f_T$ .

### Parameters $G_N^0$ and $f_T$ increase with substrate elasticity

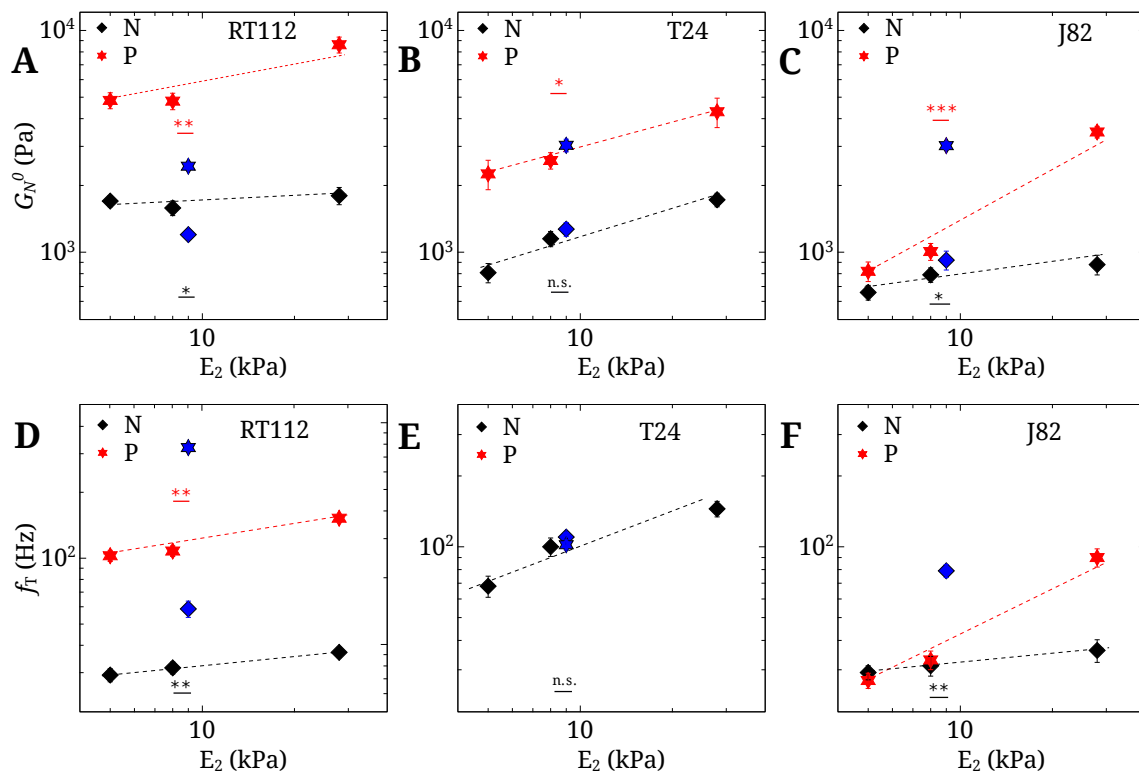


Figure 5: Parameters  $G_N^0$  (A–C) and  $f_T$  (D–F) for RT112 – T24 – J82 cancer cells, both on rigid substrates ( $E_2 = 5, 8, 28$  kPa) and HUVEC monolayer ( $E_2 \sim 9$  kPa). P = Perinuclear region (red stars), N = Nucleus (black diamonds).  $n = 5$ , error bars represent SEM. The blue points represent data on the HUVEC substrate. Lines are just a guide for the eye. Statistical relevances of  $G_N^0$  and  $f_T$  are shown when comparing the HUVEC substrate with the gel of rigidity  $E_2 = 8$  kPa.

In order to quantify the changes highlighted in the previous part, two parameters were studied, namely the plateau modulus  $G_N^0$  (Fig. 5 A–C) and the transition frequency  $f_T$  (Fig. 5 D–F). These parameters were defined earlier in Eq. 6. Their evolution is shown at locations N and P for all cell types. To compare results on HUVECs and gels, we assume that  $E_2 \sim 3 G_N^0 \sim 9$  kPa, for endothelial cells (51). Fig. 5 represents the evolution of  $G_N^0$  and  $f_T$  in terms of elasticity  $E_2$ , with HUVECs being close to the elastic substrate  $E_2 = 8$  kPa. Justification of the model for the endothelial monolayer as a thin substrate can be

found in Appendix C of the Supporting Material.  $G_N^0$  and  $f_T$  both increase linearly (log–log scale) with substrate rigidity  $E_2$ , at a higher rate for location P, as compared to N. One could expect the HUVEC data to lie along the evolution curve. On the contrary, the values found for  $G_N^0$  and  $f_T$  are quite different from the ones expected for an equivalent elastic substrate.  $G_N^0$  is higher in the perinucleus region (P) than on the nucleus (N). With the HUVEC monolayer,  $G_N^0$  is higher than expected for J82, equal for T24 and lower for RT112 cells. Finally, regarding  $f_T$  (when defined), differences are also found on the HUVECs: RT112 exhibits larger  $f_T$ , T24 value exists only on HUVECs at the perinucleus (P) and  $f_T$  for invasive J82 cells shows a large change on the nucleus (N) but is not defined on the perinucleus (P). The presence of the endothelium (HUVEC) shows indeed differences that could have been expected, due to the different nature of the substrates, both in terms of cytoskeleton, as well as adhesion molecules. Thus the next section investigates the dynamic behavior of J82 cancer cells in contact with the endothelium, until transmigration is achieved. The actin cytoskeleton organization (52) will be followed, and linked with microrheological changes observed above.

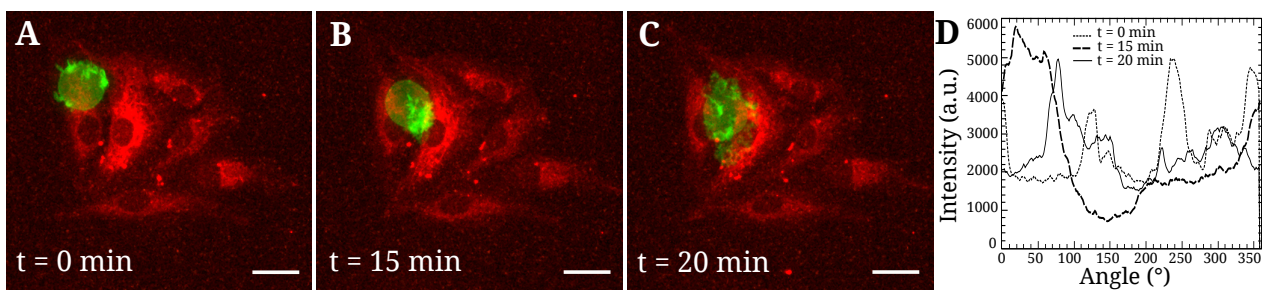


Figure 6: Transmigration of a J82 cancer cell (green) in contact with the endothelium (red). (A) Initially the cell is round ( $t = 0$  min) with actin concentrated at the periphery, (B) followed by an ovoid shape with actin relocation close to the endothelial gap ( $t = 15$  min), (C) then it transmigrates and spreads below the endothelium ( $t = 20$  min). Scale bar =  $25 \mu\text{m}$ . (D) Polar representations of the actin intensity at the cell edge measured from the center of geometry, at different times. Note in particular the large actin area for  $t = 15$  min.

### Transendothelial migration requires actin reorganization of cancer cells

When cancer cells are in contact with the endothelium substrate, they may possibly transmigrate (3), so it is important to understand how they adapt their actin cytoskeleton. This effect could be related to the mechanical features shown previously, and to mechanosensitivity. One example of these features is shown in Fig. 6. Cancer cells are let to sediment and to adhere to endothelial cells patterns. We select one pattern with only one cancer cell adhering, and followed it when interacting with the HUVEC monolayer. The cell shape and actin organization can be seen during the course of transmigration. Initially, the cell is round ( $t = 0$ , Fig. 6 A) and the actin seems to be concentrated on the sides. This local concentration can be linked to the cell mechanical properties, as measured above. Then the cell becomes ovoid ( $t = 15$  min, Fig. 6 B) and actin seems to relocate close to the junction, as if the cell was pushing harder to penetrate. Finally the cell squeezes through the junction and is found below the endothelial monolayer ( $t = 20$  min, Fig. 6 C) where it has spread. Fig. 6 D also shows the polar distribution of actin

along the cell edge. At time  $t = 15$  min, there is indeed a very large actin concentration in the  $[0 - 70^\circ]$  angular range, close to the endothelial gap.

## DISCUSSION

The choice of bladder cancer cells comes from previous studies by the authors (39–41), where various properties associated with invasiveness, such as adhesion and rheology, were reported. RT112 cancer cells are moderately differentiated while T24 and J82 cancer cells are poorly differentiated and have a higher malignancy potential (especially J82 cells). In addition, these cancer cells were used before as models for molecular classification (53). They exhibited various expression degrees of mTOR-associated genes, relevant for chemotherapy. Adhesion molecules or ligands (CD43, MUC-1) present at the cancer cell surface have been identified (40, 41, 54) as well as receptors (ICAM-1, VCAM-1) on the HUVEC side (39). Note that CD43 (Leukosialin) and MUC-1 (Mucin 1) are expressed more on invasive cells especially T24 and J82 cell lines. When plated on gels functionalized with fibronectin, cancer cell receptors are more likely to be  $\alpha_v\beta_3$  or  $\alpha_5\beta_1$  integrins (55) interacting with the extra-cellular matrix (fibronectin). In addition, the expressions of  $\alpha_5$  and  $\beta_1$  are particularly relevant for cancer cells such as T24 (56). Finally, during the process of metastasis, it was shown that the NF $\kappa$ -B pathway can be involved in the overexpression of adhesion molecules (39).

### Rheological data corrections

The effect of a cell adhering on a rigid substrate has been investigated previously and corrections have been proposed (13, 14, 46). But softer substrates, with rigidity close to that of the cell, can also play a role, therefore it is necessary to account for the effect of both substrates, the soft one with elasticity  $E_2$  and the rigid one with elasticity  $E_3$  (glass for instance) to determine  $E_1$ , the cell elastic modulus, when the environment has different stiffnesses or thicknesses. Here we used a previous model (48) to investigate these properties numerically, taking into account the exact tip shape, a rounded cone, as considered earlier by other authors (57). An important result is that, depending on substrate stiffness, cell modulus  $E_1$  can be overestimated (when  $E_1 < E_2$ ) or underestimated (when  $E_1 > E_2$ ), this being illustrated in Fig. S1 of the Supporting Material: the effective modulus can be a decreasing or increasing function of the reduced indentation. The other important parameters are the indentation  $\delta$ , cell height  $h_1$  and substrate thickness  $h_2$ . Note that the spreading of cells on soft gels was studied earlier (22) when gel thickness was varied, in the particular case of mesenchymal stem cells. Cells spread more when the thickness  $h_2$  decreased, and cell area leveled out for high thicknesses. This latter statement is in agreement with our model at small indentations (or large heights) as the apparent stiffness also shows a plateau in Fig. S1, corresponding to the expected modulus. Finally, our model was applied to dynamic rheology and linearized in Eq. 5 to obtain the complex dynamic viscoelastic modulus  $G^*$ , accounting for substrate effects, including both viscoelasticity and thickness. Validation of the model in simple cases can be found in Appendix B of the Supporting Material.

### Cell stiffens away from nucleus

First, rheological measurements were made at different locations. Fig. 1 A–D shows the raw data obtained at positions N, P, E, indicating respectively the nucleus, perinuclear region and cell edge (see sketch as an insert in Fig. 1 B, and positions indicated in Fig. 2 C). These locations have been chosen based on geometry and microstructure considerations. The data is corrected, as explained above, due to the presence of the gel (5 kPa). Corrections are not negligible as shown by differences in the  $G'$  and  $G''$  moduli up to 40%. The final corrected value of the cell shear elastic modulus  $|G^*|$  at low frequency is around 1 kPa on the nucleus (N), thus  $E_1 \sim 3|G^*| \sim 3$  kPa. This means a stiffer substrate (5 kPa), so an overestimated value of  $|G^*|$  in the experiments. Regarding  $G''$ , the effects are more subtle, but  $G''$  increases after correction (see Appendix C in the Supporting Material). On the perinuclear region (P) or edge (E),  $|G^*| > 1.7$  kPa,  $E_1 > 5$  kPa, so the substrate is now softer, therefore  $|G^*|$  is underestimated.

After making these corrections, we note (Fig. 1 D) that the cell is stiffer when going from the center (3 kPa) to the edge (9 kPa). It is not so surprising that the center is less rigid, because the AFM tip feels the cytoskeleton as well as the nucleus at position N. Isolated nuclei are known to have a Young modulus  $E \sim 5$ –8 kPa (15), so 3 kPa is the average of nucleus, cytoplasm and membrane effects. The edge (E) or perinucleus (P), on the other hand, contain actin bundles, which are quite rigid, as observed earlier (13, 14). Disruption of actin filaments using Latrunculin A fluidifies the cytoskeleton whereas Y27632 (an actomyosin-inhibiting drug) rigidifies the cell edge (14).

#### $|G^*|$ increases with substrate stiffness $E_2$

Interesting results are presented in Fig. 1 E–H where the influence of substrate rigidity ( $E_2 = 5$ –8–28 kPa) is shown. Corrections show an increase of the modulus  $|G^*|$  after correction when  $E_2 = 5$  kPa, hardly no change for  $E_2 = 8$  kPa, and an increase for  $E_2 = 28$  kPa (Fig. 1 H). We find  $|G^*| \sim 2.5$ –3.2–4.3 kPa or  $E_1 \sim 7.5$ –9.6–13 kPa to be compared to 5–8–28 kPa respectively. We can conclude that cells adapt their rheology, i.e. are mechanosensitive. A global trend is a cell elasticity increase with substrate stiffness, and we have seen that it is related to the development of actin fibers on stiffer substrates (Fig. 2 A–C). This is in agreement with previous works (19, 20, 22, 58) and the development of stress fibers in connection with focal adhesions.

#### $|G^*|$ decreases with invasiveness as cells become glassy

The role of invasiveness on cell microrheological properties is shown in Fig. 3, using three cell types RT112, T24 and J82, by increasing order of invasiveness. When comparing measurements on the perinuclear area (P), a clear decrease in viscoelastic moduli is observed with invasiveness, both for  $G'$  and  $G''$ , and this effect persists after corrections. This confirms common trends found in the literature (5–7, 50), but more complete data is found here, because both  $G'$ ,  $G''$  as well as  $|G^*|$  are obtained in Fig. 3. In this respect, the more invasive J82 cell shows a smaller  $f_T$  (crossing of  $G'$  and  $G''$ ) around 40 Hz, revealing an earlier transition to the disordered glassy state. This was also observed for other malignant cells, like MCF-7 and MDA-MB-231 (35).

#### Most invasive cells stiffen on HUVEC monolayer



Fig. 4 illustrates measurements carried out with the three cell types on a HUVEC monolayer, at position P. This position was chosen in order to compare with PAA substrates. As cancer cells do not spread when in contact with the HUVEC monolayer (Fig. 2), only two locations (N and P) are common between gels and HUVECs. One could argue that the proteins in presence are different in both cases. Here we can assume that bonds are all strong ones, because they are receptor–ligand bonds involving integrins and fibronectin on gels, and ICAM–1 vs. other ligands (CD43 and MUC1) in the case of the HUVEC substrate (41). So the comparison can hold. To correct the data, we assume that the HUVEC monolayer behaves like a thin viscoelastic layer as explained in Appendix C of the Supporting Material. Indeed, in the range of parameters studied, the small indentation ( $\sim 500$  nm) insures no differences whatever the height of the soft substrate, so the uneven HUVEC monolayer (2–8  $\mu\text{m}$ ) is only affecting results through its viscoelastic properties, but not its height.

Data on the viscoelastic HUVEC substrate shows slightly increasing values of  $|G^*|$  with invasiveness, which is the opposite of the results found previously on gels.  $|G^*|$  increases from 3 kPa (RT112 cells) up to 3.8 kPa (J82 cells) in Fig. 4 D. To investigate these changes more accurately, we use the model described previously.

#### $G_N^0$ increases with substrate stiffness, except on HUVECs

The rheological model (14) was used to fit the data in Figs 1–3–4 to identify  $G_N^0$ , the plateau modulus, and  $f_T$ , the transition frequency. The other parameters  $a$ ,  $b$ ,  $k_0$  and  $g_1$  were also obtained but are not discussed further. To include the effect of the endothelial substrate, we used previous data on HUVECs (51) where the elasticity was found to be  $E_2 \sim 9$  kPa. This value is also included when plotting  $G_N^0$  (Fig. 5 A–C) and  $f_T$  (Fig. 5 D–F) at positions N and P. The substrates have been chosen to cover a large range of elasticities (5–28 kPa), and the evolution of  $G_N^0$  in log–log scale displays a power law, with a positive slope for position (P), as observed before when averaging different locations (23). At position (N),  $G_N^0$  seems to increase less with substrate stiffness, in agreement with indentation on the nucleus where no difference was found (18). Thus our results reconcile these two studies (18, 23) by comparing measurements at different locations. When the cells become more invasive (excluding HUVECs), the slope of  $G_N^0$  vs.  $E_2$  at position (P) seems to increase, suggesting that more invasive cell types are more mechanosensitive to gel stiffness. Finally  $f_T$  increases with  $E_2$ , therefore cells become more elastic, and do not switch to the glassy state. Note that in some cases,  $f_T$  could not be determined since there is no crossing of  $G'$  and  $G''$ .

#### Invasive J82 cells stiffen in the perinuclear area (P) on HUVECs

Finally we show that RT112 cells become less rigid on HUVECs as opposed to invasive J82 cells, especially on the perinucleus P (Fig. 5 A–C). These results are also observed on the nucleus (N) but are less visible. This could be the signature of invasive J82 cells starting to rigidify (P) in order to break through the endothelium, and let the softer nucleus (N) collapse through the endothelial gap. This process is not explained yet, although morphology changes may come from activity of the Rho–family of GTPases, controlling the cytoskeleton and acto–myosin contractility (52). In any case, this suggests a strong reorganization or mechanosensitivity of the cytoskeleton of invasive cancer cells, compatible with the current rheology data. Indeed the transition frequency  $f_T$  changes a lot on the perinucleus (P), from less invasive RT112 cells ( $f_T \sim 300$  Hz), to invasive T24 cells ( $f_T \sim 100$  Hz), and finally J82 cells show no transition (Fig. 5 D–F). This latter case is a further indication

of new dynamic organization of the cytoskeleton, corresponding to a glassy state, giving rise to the same slopes of  $G'$  and  $G''$  (17, 35, 38), and could be a signature of invasiveness. Thus we show for the first time the importance of the transition frequency  $f_T$ . This parameter, together with  $G_N^0$ , shows that few changes occur around the nucleus, as opposed to the perinuclear region, highlighting possible mechanotransduction pathways between the cytoskeleton and the nucleus, associated with linker proteins (59).

### **J82 stiffening correlates with actin reorganization during transmigration**

Finally, to illustrate the change in cancer cell mechanics when in contact with the HUVEC monolayer, transendothelial migration was followed, in order to study the relationship with microrheology measured above. Fig. 6 exhibits a J82 cancer cell transmigrating through a small pattern of HUVECs (6-8 cells). At the onset of transmigration ( $t = 0$  min, Fig. 6 A), the GFP-actin J82 cell exhibits reinforcement of its cytoskeleton at the periphery, as shown by high fluorescence intensity areas. This seems to go along with our above results and Fig. 5 showing a higher  $G_N^0$  in the perinuclear region (as compared to the nuclear region). This suggests that the cell edges are required to maintain stress at the periphery. Next the actin cortex seems to reinforce below the nucleus ( $t = 15$  min, Fig. 6 B) to push through the gap. It is not yet possible to measure this with the AFM from below, but our previous rheology data supports the dynamic nature of the cell cytoskeleton in a metastable state. Finally the cell is able to go through the gap and spread on the gel below ( $t = 20$  min, Fig. 6 C) to complete transmigration (see also Movie S1, and Appendix D in the Supporting Material). This actin reinforcement is also notable in Fig. 6 D, where the intensity indicates a very localized actin structure, corresponding to the precise location of the endothelial gap. Of course such results need to be confirmed further. In any case, this explanation provides an answer to the controversy on softer cells, as opposed to rigid ones, indicating that local rheology is essential to understand this pathological mechanism: higher rigidity on the edge is required first, followed by rapid actin reorganization to push through the gap, until the nucleus follows.

## **CONCLUSION**

In this work, we have first explained the need for correcting AFM measurements in order to obtain reliable cell viscoelastic data, which are very sensitive with respect to substrate rigidity and thickness. Our results have shown that cancer cell properties are local, vary with invasiveness, and that such cells adapt their rheology depending on substrate elasticity. In the case of an endothelial substrate, mechanosensitive effects were observed. With respect to this behavior and possible transendothelial migration leading to metastasis, invasive cancer cells exhibited locally tuned and highly dynamic mechanical properties. Further experiments are now possible to obtain real-time *in vitro* cell mechanical properties during transmigration.

## **SUPPLEMENTARY MATERIAL**

An online supplement to this article can be found by visiting BJ Online at <http://www.biophysj.org>.



## AUTHOR CONTRIBUTIONS

Y.A. performed all experiments and analyzed data. A.C. developed indentation models. V.M.L., V.S.R., R.M., V.L., A.D. and C.V. contributed analytical and experimental tools. A.D, V.M.L. and C.V. designed research. Y.A., A.D. and C.V. wrote the paper.

## ACKNOWLEDGEMENTS

We thank the ANR for grant No. 12-BS09-020-01 (TRANSMIG), the Nanoscience foundation for support of the AFM platform. This work has been partially supported by the LabeX Tec21 (Investissements d’Avenir - grant agreement No. ANR-11-LABX-0030).

## References

1. Verdier, C., J. Etienne, A. Duperray, and L. Preziosi, 2009. Review: Rheological properties of biological materials. *C. R. Acad. Sci. Phys.* 10:790–811.
2. Wirtz, D., K. Konstantopoulos, and P. C. Searson, 2011. The physics of cancer: the role of physical interactions and mechanical forces in metastasis. *Nat. Rev. Cancer* 11:512–522.
3. Chotard-Ghodsnia, R., O. Haddad, A. Leyrat, A. Drochon, C. Verdier, and A. Duperray, 2007. Morphological analysis of tumor cell/endothelial cell interactions under shear flow. *J. Biomech.* 40:335–344.
4. Weder, G., M. C. Hendriks-Balk, R. Smajda, D. Rimoldi, M. Liley, H. Heinzelmann, A. Meister, and A. Mariotti, 2014. Increased plasticity of the stiffness of melanoma cells correlates with their acquisition of metastatic properties. *Nanomedicine* 10:141–148.
5. Gück, J., S. Schinkinger, B. Lincoln, F. Wottawah, S. Ebert, M. Romeyke, D. Lenz, H. M. Erickson, R. Ananthkrishnan, D. Mitchell, J. Käs, S. Ulvick, and C. Bilby, 2005. Optical deformability as an inherent cell marker for testing malignant transformation and metastatic competence. *Biophys. J.* 88:3689–3698.
6. Cross, S. E., Y.-S. Jin, J. Rao, and J. K. Gimzewski, 2007. Nanomechanical analysis of cells from cancer patients. *Nat. Nanotechnol.* 2:780–783.
7. Lekka, M., 2016. Discrimination Between Normal and Cancerous Cells Using AFM. *Bionanoscience* 6:65–80.
8. Staunton, J. R., B. L. Doss, S. Lindsay, and R. Ros, 2016. Correlating confocal microscopy and atomic force indentation reveals metastatic cancer cells stiffen during invasion into collagen I matrices. *Sci. Rep.* 6:19686.
9. Bischofs, I. B., F. Klein, D. Lehnert, M. Bastmeyer, and U. S. Schwarz, 2008. Filamentous network mechanics and active contractility determine cell and tissue shape. *Biophys. J.* 95:3488–3496.
10. Guo, M., A. J. Ehrlicher, S. Mahammad, H. Fabich, M. H. Jensen, J. R. Moore, J. Fredberg, R. D. Goldman, and D. A. Weitz, 2013. The Role of Vimentin Intermediate Filaments in Cortical and Cytoplasmic Mechanics. *Biophys. J.* 105:1562–1568.
11. Brangwynne, C. P., F. C. MacKintosh, S. Kumar, N. A. Geisse, J. Talbot, L. Mahadevan, K. K. Parker, D. E. Ingber, and D. A. Weitz, 2006. Microtubules can bear enhanced compressive loads in living cells because of lateral reinforcement. *J. Cell Biol.* 173:733–741.
12. Rigato, A., F. Rico, F. Eghiaian, M. Piel, and S. Scheuring, 2015. Atomic force microscopy mechanical mapping of micropatterned

- cells shows adhesion geometry-dependent mechanical response on local and global scales. *ACS Nano* 9:5846–5856.
13. Santos, J. A. C., L. M. Rebêlo, A. C. Araujo, E. B. Barrosa, and J. S. de Sousa, 2012. Thickness-corrected model for nanoindentation of thin films with conical indenters. *Soft Matter* 8:4441–4448.
  14. Abidine, Y., V. M. Laurent, R. Michel, A. Duperray, and C. Verdier, 2015. Local mechanical properties of bladder cancer cells measured by AFM as a signature of metastatic potential. *Eur. Phys. J. Plus* 130:202.
  15. Caille, N., O. Thoumine, Y. Tardy, and J.-J. Meister, 2002. Contribution of the nucleus to the mechanical properties of endothelial cells. *J. Biomech.* 35:177–187.
  16. Thiam, H.-R., P. Vargas, N. Carpi, C. L. Crespo, M. Raab, E. Terriac, M. C. King, J. Jacobelli, A. S. Alberts, T. Stradal, A.-M. Lennon-Dumenil, and M. Piel, 2016. Perinuclear Arp2/3-driven actin polymerization enables nuclear deformation to facilitate cell migration through complex environments. *Nat. Commun.* 7:10997.
  17. Alcaraz, J., L. Buscemi, M. Grabulosa, X. Trepas, B. Fabry, R. Farré, and D. Navajas, 2003. Microrheology of human lung epithelial cells measured by atomic force microscopy. *Biophys. J.* 84:2071–2079.
  18. Rianna, C., and M. Radmacher, 2017. Comparison of viscoelastic properties of cancer and normal thyroid cells on different stiffness substrates. *Eur. Biophys. J.* 46:309–324.
  19. Discher, D. E., P. Janmey, and Y.-L. Wang, 2005. Tissue cells feel and respond to the stiffness of their substrate. *Science* 310:1139–1143.
  20. Lo, C. M., H. B. Wang, M. Dembo, and Y. L. Wang, 2000. Cell movement is guided by the rigidity of the substrate. *Biophys. J.* 79:144–152.
  21. Engler, A., L. Bacakova, C. Newman, A. Hategan, M. Griffin, and D. Discher, 2004. Substrate compliance versus ligand density in cell on gel responses. *Biophys. J.* 86:617–628.
  22. Buxboim, A., K. Rajagopal, A. E. X. Brown, and D. E. Discher, 2010. How deeply cells feel: methods for thin gels. *J. Physics.: Condens. Matter* 22:194116.
  23. Solon, J., I. Levental, K. Sengupta, P. C. Georges, and P. A. Janmey, 2007. Fibroblast adaptation and stiffness matching to soft elastic substrates. *Biophys. J.* 93:4453–4461.
  24. Etienne, J., J. Fouchard, D. Mitrossilis, N. Bui, P. Durand-Smet, and A. Asnacios, 2015. Cells as liquid motors: Mechanosensitivity emerges from collective dynamics of actomyosin cortex. *Proc. Natl. Acad. Sci. USA* 112:2740–2745.
  25. Acerbi, I., L. Cassereau, I. Dean, Q. Shi, A. Au, C. Park, Y. Y. Chen, J. Liphardt, E. S. Hwang, and V. M. Weaver, 2015. Human breast cancer invasion and aggression correlates with ECM stiffening and immune cell infiltration. *Integr. Biol.* 7:1120–1134.
  26. van Helvert, S., and P. Friedl, 2016. Strain stiffening of fibrillar collagen during individual and collective cell migration identified by AFM nanoindentation. *ACS Appl. Mater. Interfaces* 8:21946–21955.
  27. Alvarez-Elizondo, M. B., and D. Weihs, 2017. Cell-gel mechanical interactions as an approach to rapidly and quantitatively reveal invasive subpopulations of metastatic cancer cells. *Tissue Eng. Part C, Methods* 23:180–187.
  28. Zhu, J., L. Liang, Y. Jiao, and L. Liu, 2015. Enhanced invasion of metastatic cancer cells via extracellular matrix interface. *PLOS One* 10:e0118058.
  29. Butcher, D. T., T. Alliston, and V. M. Weaver, 2009. A tense situation: forcing tumour progression. *Nat. Rev. Cancer* 9:108–122.
  30. Jordan, A., A. Duperray, A. Gérard, A. Grichine, and C. Verdier, 2010. Breakdown of cell-collagen networks through collagen

remodeling. *Biorheology* 47:277–295.

31. Peschetola, V., V. M. Laurent, A. Duperray, R. Michel, D. Ambrosi, L. Preziosi, and C. Verdier, 2013. Time-dependent traction force microscopy for cancer cells as a measure of invasiveness. *Cytoskeleton* 70:201–214.
32. Mierke, C. T., D. Rösel, B. Fabry, and J. Brábek, 2008. Contractile forces in tumor cell migration. *Eur. J. Cell Biol.* 87:669–676.
33. Koch, T. M., S. Münster, N. Bonakdar, J. P. Butler, and B. Fabry, 2012. 3D Traction forces in cancer cell invasion. *PLOS One* 7:e33476.
34. Smith, B. A., B. Tolloczko, J. G. Martin, and P. Grütter, 2005. Probing the viscoelastic behavior of cultured airway smooth muscle cells with atomic force microscopy: stiffening induced by contractile agonist. *Biophys. J.* 88:2994–3007.
35. Rother, J., H. Nöding, I. Mey, and A. Janshoff, 2014. Atomic force microscopy-based microrheology reveals significant differences in the viscoelastic response between malign and benign cell lines. *Open Biology* 4:140046.
36. Abidine, Y., V. M. Laurent, R. Michel, A. Duperray, L. Palade, and C. Verdier, 2015. Physical properties of polyacrylamide gels probed by AFM and rheology. *Europhys. Letters* 109:38003.
37. Korsunsky, A. M., and A. Constantinescu, 2009. The influence of indenter bluntness on the apparent contact stiffness of thin coatings. *Thin Solid Films* 517:4835–4844.
38. Trepap, X., G. Lenormand, and J. J. Fredberg, 2008. Universality in cell mechanics. *Soft Matter* 4:1750–1759.
39. Haddad, O., R. Chotard-Ghodnsnia, C. Verdier, and A. Duperray, 2010. Tumor cell/endothelial cell tight contact upregulates endothelial adhesion molecule expression mediated by NFκB: differential role of the shear stress. *Exp. Cell Research* 316:615–626.
40. Laurent, V. M., A. Duperray, V. R. Sundar, and C. Verdier, 2014. Atomic Force Microscopy Reveals a Role for Endothelial Cell ICAM-1 Expression in Bladder Cancer Cell Adherence. *Plos One* 9:e98034.
41. Rajan, V. S., V. M. Laurent, C. Verdier, and A. Duperray, 2017. Unraveling the Receptor-Ligand Interactions between Bladder Cancer Cells and the Endothelium Using AFM. *Biophys. J.* 112:1246–1257.
42. Palecek, S. P., J. C. Loftus, M. H. Ginsberg, D. A. Lauffenburger, and A. F. Horwitz, 1997. Integrin-ligand binding properties govern cell migration speed through cell-substratum adhesiveness. *Nature* 385:537–540.
43. Grevesse, T., M. Versaevel, G. Circelli, S. Desprez, and S. Gabriele, 2013. A simple route to functionalize polyacrylamide hydrogels for the independent tuning of mechanotransduction cues. *Lab. Chip* 13:777–780.
44. Butt, H.-J., and M. Jaschke, 1995. Calculation of thermal noise in atomic force microscopy. *Nanotechnology* 6:1–7.
45. Bilodeau, G. G., 1992. Regular pyramid punch problem. *J. Appl. Mech.* 59:519–523.
46. Dimitriadis, E. K., F. Horkay, J. Maresca, B. Kachar, and R. S. Chadwick, 2002. Determination of elastic moduli of thin layers of soft material using the atomic force microscope. *Biophys. J.* 82:2798–2810.
47. Korsunsky, A. M., and A. Constantinescu, 2006. Work of indentation approach to the analysis of hardness and modulus of thin coatings. *Materials Sci. Eng. A* 423:28–35.
48. Constantinescu, A., A. Korsunsky, O. Pison, and A. Oueslati, 2013. Symbolic and numerical solution of the axisymmetric indentation problem for a multilayered elastic coating. *Int. J. Solids Struct.* 50:2798–2807.
49. Stamenovic, D., N. Rosenblatt, M. Montoya-Zavala, B. D. Matthews, S. Hu, B. Suki, N. Wang, and D. E. Ingber, 2007. Rheological behavior of living cells is timescale-dependent. *Biophys. J.* 93:L39–L41.
50. Lekka, M., J. Lekki, M. Marszalek, P. Golonka, Z. Stachura, B. Cleff, and A. Hryniewicz, 1999. Local elastic properties of cells studied by SFM. *Appl. Surf. Sci.* 141:345–349.

51. Abidine, Y., 2015. Propriétés mécaniques de cellules cancéreuses mesurées par AFM. Ph.D. thesis, Université Grenoble Alpes.
52. Reymond, N., B. B. d'Água, and A. J. Ridley, 2013. Crossing the endothelial barrier during metastasis. *Nature Rev. Cancer* 13:858–870.
53. Hau, A. M., M. Nakasaki, K. Nakashima, G. Krish, and D. E. Hansel, 2017. Differential mTOR pathway profiles in bladder cancer cell line subtypes to predict sensitivity to mTOR inhibition. *Urologic Oncology* S1078-1439 (17):30134–5.
54. Kaur, S., N. Momi, S. Chakraborty, D. G. Wagner, A. J. Horn, S. M. Lele, D. Theodorescu, and S. K. Batra, 2014. Altered expression of transmembrane mucins, MUC1 and MUC4, in bladder cancer: pathological implications in diagnosis. *PLoS One* 9:e92742.
55. Kang, H. W., W.-J. Kim, and S. J. Yun, 2017. The role of the tumor microenvironment in bladder cancer development and progression. *Transl. Cancer Res.* 6(S4):744–758.
56. Saito, T., M. Kimura, T. Kawasaki, S. Sato, and Y. Tomita, 1996. Correlation between integrin alpha 5 expression and the malignant phenotype of transitional cell carcinoma. *British J. Cancer* 73:327–331.
57. Rico, F., P. Roca-Cusachs, N. Gavara, R. Farré, M. Rotger, and D. Navajas, 2005. Probing mechanical properties of living cells by atomic force microscopy with blunted pyramidal cantilever tips. *Phys. Rev. E* 72:021914.
58. Trichet, L., J. Le Digabel, R. J. Hawkins, S. R. K. Vedula, M. Gupta, C. Ribault, P. Hersen, R. Voituriez, and B. Ladoux, 2012. Evidence of a large-scale mechanosensing mechanism for cellular adaptation to substrate stiffness. *Proc. Natl. Acad. Sci. USA* 109:6933–6938.
59. Guilluy, C., L. D. Osborne, L. Van Landeghem, L. Sharek, R. Superfine, R. Garcia-Mata, and K. Burridge, 2014. Isolated nuclei adapt to force and reveal a mechanotransduction pathway in the nucleus. *Nat. Cell Biol.* 16:376–381.

**Biophysical Journal, Volume xxx**

**Supplemental Information**

**Mechanosensitivity of cancer cells in contact with soft substrates using AFM**

**Y. Abidine, A. Constantinescu, V.M. Laurent, V. Sundar Rajan, R. Michel, V. Laplaud, A. Duperray, and C. Verdier**

## Supporting Material

### Appendix A: Numerical simulations of indentation with a three-layer model

The corrected Hertz formula for the apparent elastic modulus obtained by the indentation of a three-layer substrate proposed in Eq. 2 was assessed using the numerical model for indentation of a multilayered substrate (48). The computations are based on (i) the Papkovitch-Neuber potential description of the displacements field in each layer, (ii) displacement and traction continuity across the interfaces and (iii) a frictionless contact condition using the exact shape of a rigid indenter. However several algorithmic details have been adapted to the precise shape of the AFM indenter, i.e. a rounded cone with a sharp angle of 20 degrees. The sharp angle imposed a novel estimation of the apparent contact modulus based on the geometry of the rounded cone, i.e. combining the spherical shape with a vertically shifted cone, whereas in (37, 48) only the cone was used. Moreover the starting point and the algorithm for the computation of the contact area have also been modified to insure a fast and robust convergence.

A typical example of indentation of a three-layer substrate using the AFM tip with elastic moduli and layer thicknesses of the discussed experiment is displayed in Fig. S1. The picture displays several characteristic features of the indentation of a layered medium and is coherent with experimental observations and theoretical expectations. One can remark that values of the apparent contact modulus at small indentation depth converge to the value of the apparent contact modulus of the first layer. Note that the apparent contact modulus of a material also depends on the Poisson coefficient and is not equal to the Young modulus of the material. This convergence to the apparent contact modulus was obtained after corrections based on the exact shape of the AFM indenter as explained before.

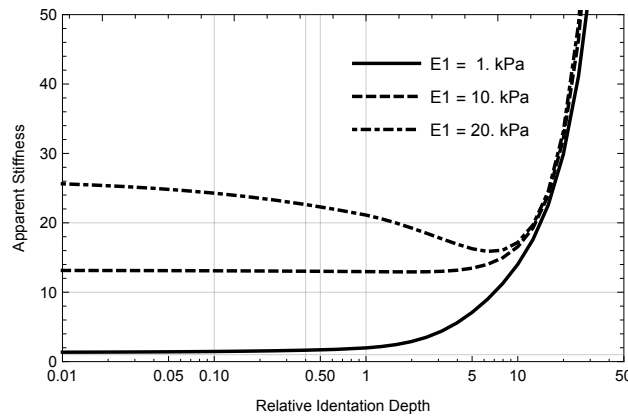


Figure S1: LogNormal plot of the apparent contact modulus  $\bar{E}$  vs. reduced indentation depth  $\delta/h_{12}$  for different moduli of the first layer  $E_1 = 1, 10, 20$  kPa (cell) and a second layer of  $E_2 = 8$  kPa (gel) on a very rigid substrate  $E_3 = 70$  MPa (glass).  $h_1 = 10 \mu\text{m}$  and  $h_2 = 70 \mu\text{m}$ . Note the minimum of the curve when  $E_1 > E_2$ .

Furthermore, the model predicts the apparent contact modulus of the first layer correctly even when the second layer is softer. In addition, the apparent contact modulus presents in this case a minimum located in the second layer zone as expected.

Let us further present the approximation of the correction of the Hertz formula for a three-layer system. One can first consider the apparent contact modulus  $\bar{E}_{12}$  of the double layer (made of layers 1 and 2), which can be decomposed as in (37):

$$\bar{E}_{12(\delta)} = \bar{E}_2 + \frac{\bar{E}_1 - \bar{E}_2}{1 + \left(\frac{\delta}{\beta_0 h_1}\right)^{\eta_0}} \quad (8)$$

where  $\bar{E}_1 = \frac{E_1}{1-\nu_1^2}$ ,  $\bar{E}_2 = \frac{E_2}{1-\nu_2^2}$  and  $\beta_0, \eta_0$  are adjusting constants. Constructing a similar formula, by adding the substrate (layer 3), leads to the final representation of the apparent modulus  $\bar{E}_{(\delta)}$ :

$$\bar{E}_{(\delta)} = \bar{E}_3 + \frac{\bar{E}_{12} - \bar{E}_3}{1 + \left(\frac{\delta}{\beta_1 h_{12}}\right)^{\eta_1}} \quad (9)$$

where  $\bar{E}_3 = \frac{E_3}{1-\nu_3^2}$  is the apparent modulus of the substrate,  $h_{12} = h_1 + h_2$  is the combined height of the two layers and  $\beta_1$  and  $\eta_1$  are adjusting parameters. Combining Eq. 8 and Eq. 9, one obtains using simple algebra:

$$\bar{E}_{(\delta)} = \bar{E}_3 + \frac{\bar{E}_2 + \frac{\bar{E}_1 - \bar{E}_2}{1 + \left(\frac{\delta}{\beta_0 h_1}\right)^{\eta_0}} - \bar{E}_3}{1 + \left(\frac{\delta}{\beta_1 h_{12}}\right)^{\eta_1}} \quad (10)$$

The adjusting parameters, i.e.  $\beta_0, \eta_0, \beta_1$  and  $\eta_1$ , are obtained by fitting the apparent contact modulus in Eq. 10 with the numerical results using a least square method. Two typical adjustments are displayed in Fig. S2 A and B.

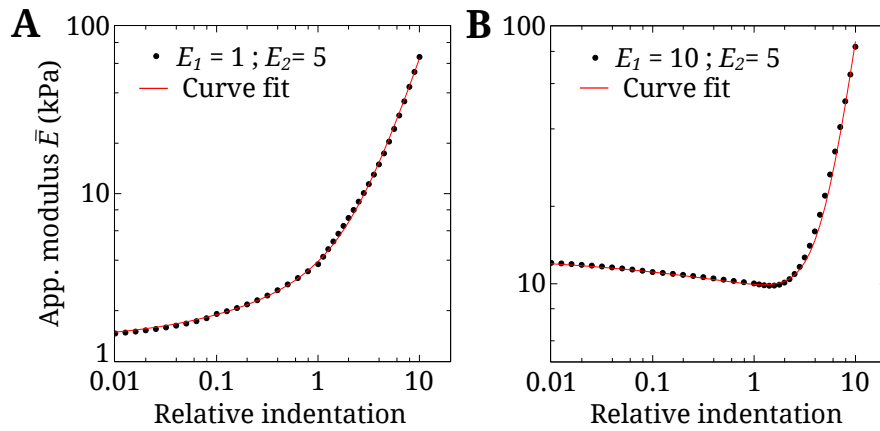


Figure S2: Comparison of the apparent contact modulus  $\bar{E}_{(\delta)}$  obtained from the three-layer model (*points*) and Eq. 10 (*line*). (A)  $E_1 = 1$  kPa,  $E_2 = 5$  kPa (and  $E_3 = 70$  MPa). The fitted parameters for this curve are  $\beta_0 = 3.7$ ,  $\eta_0 = 0.6$ ,  $\beta_1 = 5.9$  and  $\eta_1 = 1.8$ . (B)  $E_1 = 5$  kPa,  $E_2 = 10$  kPa (and  $E_3 = 70$  MPa). The fitted parameters for this curve are  $\beta_0 = 1.55$ ,  $\eta_0 = 0.38$ ,  $\beta_1 = 109$  and  $\eta_1 = 2.88$ .

The four fitting parameters  $\beta_0, \eta_0, \beta_1$  and  $\eta_1$  are obtained and plotted against  $E_1$ . Fits are made, to be used in the iteration procedure, as explained in Appendix B below.

## Appendix B: Linearization of the modified Hertz model of indentation

Once analytical relations for  $\bar{E}(\delta)$  have been found, a linearization can be done. The indentation force  $F_0$  applied to our sample, as a function of the indentation  $\delta_0$ , is:

$$F_0 = \frac{3}{4} \bar{E}_{(\delta_0)} \tan \theta \delta_0^2 \quad (11)$$

where  $\theta$  is the pyramid half-angle. A small oscillatory amplitude  $\delta$  is superposed to the indentation  $\delta_0$ . Eq. 11 becomes:

$$F_0 + F = \frac{3}{4} \bar{E}_{(\delta_0+\delta)} \tan \theta (\delta_0 + \delta)^2 \quad (12)$$

Only terms of the first order are kept, therefore:

$$\frac{F}{\delta} = \frac{3}{2} \tan \theta \delta_0 [\bar{E}_{(\delta_0)} + \frac{\delta_0}{2} \bar{E}'_{(\delta_0)}] \quad (13)$$

Let us now differentiate the apparent modulus  $\bar{E}(\delta)$  with respect to the indentation  $\delta$ , from Eq. 10:

$$\begin{aligned} \bar{E}'_{(\delta)} = \frac{d\bar{E}}{d\delta} &= \frac{1}{[1 + (\frac{\delta}{\beta_1 h_{12}})^{\eta_1}]^2} \times \\ &\frac{1}{\delta} \left[ (\bar{E}_2 - \bar{E}_1) \eta_0 \left(\frac{\delta}{\beta_0 h_1}\right)^{\eta_0} \frac{1 + (\frac{\delta}{\beta_1 h_{12}})^{\eta_1}}{(1 + (\frac{\delta}{\beta_0 h_1})^{\eta_0})^2} + \eta_1 \left(\frac{\delta}{\beta_1 h_{12}}\right)^{\eta_1} (\bar{E}_3 - \bar{E}_2 - \frac{\bar{E}_1 - \bar{E}_2}{1 + (\frac{\delta}{\beta_0 h_1})^{\eta_0}}) \right] \end{aligned} \quad (14)$$

Introducing the following variables  $\chi_0 = \frac{\delta_0}{\beta_0 h_1}$  and  $\chi_1 = \frac{\delta_0}{\beta_1 h_{12}}$ , the apparent modulus in Eq. 10 is evaluated at  $\delta_0$ :

$$\bar{E}_{(\delta_0)} = \frac{\bar{E}_1 + \bar{E}_2 \chi_0^{\eta_0} + \bar{E}_3 (1 + \chi_0^{\eta_0}) \chi_1^{\eta_1}}{(1 + \chi_0^{\eta_0})(1 + \chi_1^{\eta_1})} \quad (15)$$

and  $\bar{E}'_{(\delta)}$  from Eq. 14 is evaluated at  $\delta = \delta_0$ :

$$\begin{aligned} \bar{E}'_{(\delta_0)} = \frac{d\bar{E}}{d\delta}_{(\delta_0)} &= \frac{1}{[1 + \chi_1^{\eta_1}]^2} \frac{1}{\delta_0} \times \\ &(-\bar{E}_1 \left[ \eta_0 \chi_0^{\eta_0} \frac{1 + \chi_1^{\eta_1}}{(1 + \chi_0^{\eta_0})^2} + \eta_1 \chi_1^{\eta_1} \frac{1}{1 + \chi_0^{\eta_0}} \right] + \bar{E}_2 \left[ \eta_0 \chi_0^{\eta_0} \frac{1 + \chi_1^{\eta_1}}{(1 + \chi_0^{\eta_0})^2} - \eta_1 \chi_1^{\eta_1} \frac{\chi_0^{\eta_0}}{1 + \chi_0^{\eta_0}} \right] + \bar{E}_3 [\eta_1 \chi_1^{\eta_1}]) \end{aligned} \quad (16)$$

Now let us replace the apparent modulus  $\bar{E}(\delta_0)$  and  $\bar{E}'_{(\delta_0)}$  from Eq. 15–16 into Eq. 13. We obtain:

$$\frac{F}{\delta} \frac{2}{3 \tan \theta \delta_0} = \bar{E}_1 k_1(\chi_0, \chi_1) + \bar{E}_2 k_2(\chi_0, \chi_1) + \bar{E}_3 k_3(\chi_1) \quad (17)$$



where we have defined:

$$\begin{cases} k_1(\chi_0, \chi_1) = \frac{2(1 + \chi_0^{\eta_0})(1 + \chi_1^{\eta_1}) - \eta_0 \chi_0^{\eta_0}(1 + \chi_1^{\eta_1}) + \eta_1 \chi_1^{\eta_1}(1 + \chi_0^{\eta_0})}{2(1 + \chi_0^{\eta_0})^2(1 + \chi_1^{\eta_1})^2} \\ k_2(\chi_0, \chi_1) = \frac{2\chi_0^{\eta_0}(1 + \chi_0^{\eta_0})(1 + \chi_1^{\eta_1}) + \eta_0 \chi_0^{\eta_0}(1 + \chi_1^{\eta_1}) - \eta_1 \chi_1^{\eta_1} \chi_0^{\eta_0}(1 + \chi_0^{\eta_0})}{2(1 + \chi_0^{\eta_0})^2(1 + \chi_1^{\eta_1})^2} \\ k_3(\chi_1) = \frac{\chi_1^{\eta_1}(2 + \eta_1 + 2\chi_1^{\eta_1})}{2(1 + \chi_1^{\eta_1})^2} \end{cases} \quad (18)$$

It is now possible to obtain the apparent moduli  $\bar{E}_1$  from Eq. 17:

$$\bar{E}_1 = \frac{F}{\delta} \frac{2}{3 k_1 \tan \theta \delta_0} - \bar{E}_2 \frac{k_2}{k_1} - \bar{E}_3 \frac{k_3}{k_1} \quad (19)$$

Using  $E_1 = 2 G_1 (1 + \nu_1)$ , and the expressions of  $\bar{E}_1$ ,  $\bar{E}_2$  and  $\bar{E}_3$ , Eq. 19 can be rewritten:

$$G_1 = \frac{F}{\delta} \frac{1 - \nu_1}{3 \tan \theta \delta_0} \frac{1}{k_1} - E_2 \frac{k_2}{k_1} \frac{1 - \nu_1}{2(1 - \nu_2^2)} - E_3 \frac{k_3}{k_1} \frac{1 - \nu_1}{2(1 - \nu_3^2)} \quad (20)$$

Let us introduce the complex force  $F^*(\omega)$  and indentation  $\delta^*(\omega)$ ; the complex shear modulus  $G^*(\omega)$  of the first layer is:

$$G_1(\omega) = G_1^*(\omega) = \frac{F^*(\omega)}{\delta^*(\omega)} \frac{1 - \nu_1}{3 \tan \theta \delta_0} \frac{1}{k_1} - E_2^* \frac{k_2}{k_1} \frac{1 - \nu_1}{2(1 - \nu_2^2)} - E_3^* \frac{k_3}{k_1} \frac{1 - \nu_1}{2(1 - \nu_3^2)} \quad (21)$$

where  $E_2^*$  and  $E_3^*$  can also be complex. When using elastic gels, we use  $E_2^* = E_2$  which is real. When using endothelial cells,  $E_2^*$  is complex and was measured separately. Finally  $E_3^* = E_3$  is real for the glass substrate. Eq. 21 is used to determine  $G^*(\omega)$  based on an iterative process. This requires to initiate with a given value of  $G_1^*$  (close to previous ones), determine  $k_1$ , and plug it into the right hand side of Eq. 21 to find the new  $G^* = G_1^*$ . A few iterations (around twenty usually) are necessary to converge to the desired value  $G^*(\omega)$ .

### Appendix C: Influence of substrate rheology and thickness

Simulations were carried out to characterize the influence of the substrate rheology and height in the three-layer model described in our study. Here we considered an apparent shear complex modulus  $G_1^*(\omega)$  for the first layer ( $G_1^* = G_{cell}^*$ ), and calculated the corrected modulus  $G_{cor}^*(\omega)$  depending on different parameters of the substrate.

As an example,  $G_1^*(\omega)$  is generated using the simplified fitting model described in Eqs. 6–7, with the following values of the parameters:  $G_N^0 = 2000$  Pa,  $n_f = 0.1$ ,  $k_0 = 200$  Pa,  $g_1 = 5$ ,  $a = 1.2$ ,  $b = 1.5$ , consistent with classical cell data. Thus, the value of the modulus  $|G_1^*|^1$  at low frequencies is  $|G_1^*(1Hz)| \sim 2$  kPa and  $E_1 \sim 3 |G_1^*(1Hz)| \sim 6$  kPa.

The three different gels used in our study ( $E_2 = 5, 8, 28$  kPa) were considered. Then an elastic substrate as well as a viscoelastic substrate were simulated. Finally, the sensibility to the height of the substrate was studied using three different

<sup>1</sup>The modulus of the complex shear modulus  $G^*$  is  $|G^*| = (G'^2 + G''^2)^{1/2}$

values  $h_2 = 2, 8, 70 \mu\text{m}$ . In all these cases, the height  $h_1 = 1 \mu\text{m}$  of the first layer (the cell) and the indentation  $\delta = 400 \text{ nm}$  of the tip were kept constant.

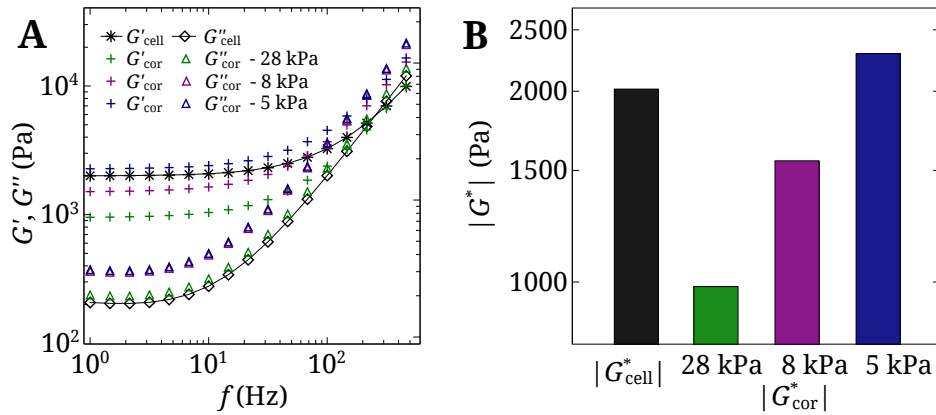


Figure S3: Substrate correction when the substrate has an elastic modulus  $E_2$  higher, close to or smaller than the elastic modulus  $E_1 = 6 \text{ kPa}$  of the first layer (cell). (A) Generated viscoelastic moduli of the cell  $G_1^* = G_{cell}^*$  (black), and corrected viscoelastic moduli considering three values of  $E_2 = 5, 8, 28 \text{ kPa}$ . (B)  $|G_{cell}^*|$  and the corresponding values of  $|G_{cor}^*|$  calculated at 1 Hz. In this simulation,  $h_2 = 70 \mu\text{m}$ ,  $h_1 = 1 \mu\text{m}$ , and  $\delta = 400 \text{ nm}$ .

### Influence of the substrate elasticity

Fig. S3 shows the influence of the second layer elastic modulus  $E_2$  on the viscoelastic properties of the first layer ( $G_1^* = G_{cell}^*$ ). The results can be summarized as follows, using  $E_{cell} = 3 |G_{cell}^*|$ :

- If  $E_{cell} > E_2$ , the cell rigidity is underestimated because of the presence of a softer substrate below. Thus the correction increases the values of  $G'$  and  $G''$  (Fig. S3 A, blue symbols).

- If  $E_{cell} < E_2$ , the cell rigidity is overestimated because of the presence of a more rigid substrate below, and the correction lowers the values of  $G'$  (Fig. S3 A, purple and green symbols). On the other hand, the effect on  $G''$  depends non linearly on  $E_2$ .

The higher  $E_2$ , the higher the correction (see larger correction of  $E_2 = 28 \text{ kPa}$  as compared to  $E_2 = 5$  and  $8 \text{ kPa}$ ). These results are summarized in Fig. S3 B where the shear modulus  $|G_{cor}^*|$  at 1 Hz is represented in the three cases.

### Comparison between an elastic substrate and a viscoelastic substrate

When we considered a viscoelastic substrate with high values of  $G''$  (like the layer of HUVECs, Fig. S4 A), the cell viscous component was affected as follows:

- If  $G_{cell}'' > G_{substrate}''$ , the cell viscous component is underestimated, and the correction increases  $G_{cell}''$ .

- If  $G_{cell}'' < G_{substrate}''$ , the cell viscous component is overestimated, and the correction decreases  $G_{cell}''$  as shown in

Fig. S4 B (turquoise).

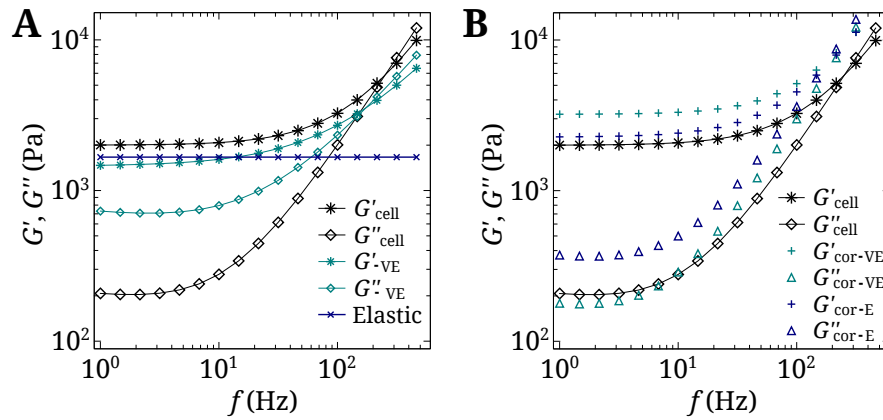


Figure S4: Correction of the apparent modulus  $G_{cell}^*$  considering an elastic substrate and a viscoelastic one. (A) Apparent viscoelastic moduli of the cell  $G_{cell}^*$  (black), of the substrate  $G_{VE}^*$  (turquoise) with  $|G_2^*(1Hz)| = 1.7$  kPa, and corresponding elastic substrate  $E_2 = 5$  kPa  $\sim 3|G_2^*(1Hz)|$  kPa (blue). The viscoelastic moduli of the substrate were generated using the fitting model. (B) Corrected viscoelastic moduli considering the viscoelastic substrate (turquoise) and the elastic substrate (blue).

Considering only an equivalent elastic substrate (same  $|G_2^*(1Hz)| = 1.7$  kPa,  $E_2 \sim 5$  kPa) gave rise to different  $G'$  and  $G''$  (blue). Therefore the precise contribution of the viscoelasticity of the substrate is important as it affects both  $G'$  and  $G''$ .

### Influence of substrate height – Justification of the HUVEC thin layer model

Fig. S5 shows the effect of substrate height  $h_2$  when cells are in contact with an 8 kPa thin layer. In this case, the high value of  $E_2$  leads to overestimation of the moduli  $G'$  and  $G''$ , so a diminution of  $h_2$  increases substrate effects, lowering  $G'$  and  $G''$ . But the correction is very small.

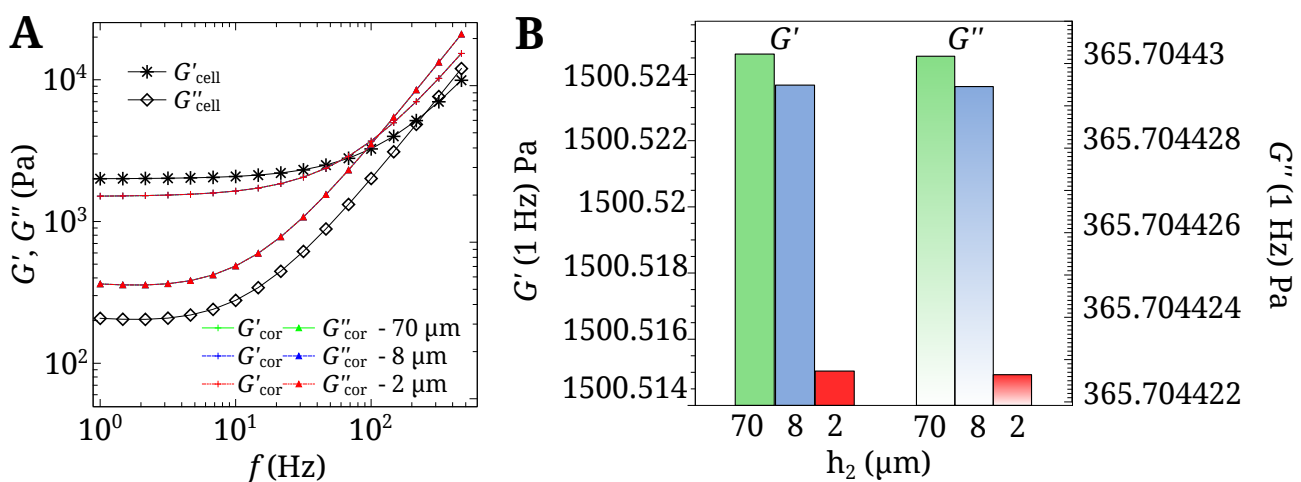


Figure S5: Correction of the apparent modulus  $G_{cell}^*$  considering three different substrate heights  $h_2 = 2, 8, 70 \mu m$ . The other parameters are:  $E_2 = 8$  kPa,  $h_1 = 1 \mu m$  and  $\delta = 0.4 \mu m$ .

This is due to the fact that the relative indentation depth  $\frac{\delta}{h_{12}}$  is always very small in this case. Indeed, as shown in [Fig. S1](#), the apparent stiffness remains almost constant for small relative indentation depths (lower than 0.1), which is the case in most experiments involving the HUVEC monolayer simulated here. The correction mainly comes here from the elasticity  $E_2$  of the underlying substrate ( $E_2 = 8$  kPa), as already seen in [Fig. S3 B](#), but the thickness is not so important. This is a justification of our approach of the endothelial layer, which can be mimicked by a thin layer, even though it has a waviness corresponding to hollows and bumps (thickness between 2 and 8  $\mu\text{m}$ ). Therefore we can assume that the substrate height does not influence much the corrected values of the viscoelastic moduli.

#### **Appendix D: Cancer cell transmigration through the endothelium**

[Movie S1](#) provides adequate evidence of the cancer cell passage through the endothelium.

**Transmigration of cancer cell.** A J82 cancer cell is tagged with Actin–GFP (green) and endothelial cells (purple) are stained using CellTrace Far Red DDAO-SE from Life technologies. Beads also appear in red and indicate the gel (8 kPa) upper surface. At the beginning of transmigration, the endothelial cells are seen from below showing no trace of tumor cell. Then a view from the side shows the dynamic process followed by the cancer cell, penetrating through the endothelial monolayer. At the end, a view from below shows the cancer cell (green) after eventually passing through the endothelium.